PROCEEDINGS, 41st Workshop on Geothermal Reservoir Engineering
Stanford University, Stanford, California, February 22-24, 2016
SGP-TR-209

Laboratory and Numerical Evaluation of EGS Shear Stimulation

Stephen Bauer[1], Kai Huang[2], Qinglu Chen[2], Ahmad Ghassemi[2] , Perry Barrow[1]

[1]Sandia National Laboratories

[2]The University of Oklahoma, Norman, OK

sjbauer@sandia.gov

ahmad.ghassemi@ou.edu

Keywords: shear stimulation, thermal stress, numerical analysis, experimental rock deformation

Abstract

This paper presents the results of an experimental program along with numerical modeling to study shear stimulation of fractures in response to cold water injection. Laboratory-based experimental and numerical analysis results are used to provide a physics-based understanding of shear stimulation phenomena (hydroshearing) and its evolution during stimulation. In order to study hydroshearing in the laboratory, a test system has been configured to (1) simulate reasonable downhole EGS environmental conditions, (2) flow cool water along fractures in hot and stressed fractured rock, (3) from (2) promote slip, (4) model the experiments in a tractable manner such that insight may be obtained of slip mechanisms. Thermo-poroelastic finite element analysis of a fractured rock injection experiment has been carried out to explore the role of pore pressure, cooling and coupled processes on fracture deformation and slip. Good agreement between modeling and experimental observations is achieved. Simulation results illustrate that pore pressure and cooling cause the fracture system to deform resulting in permeability modifications. Fracture permeability evolution with stress variations in the sample is also observed in these experiments.

1. INTRODUCTION

For engineered geothermal systems (EGS), self-propping shear stimulation, sometimes called hydroshearing, of existing fracture networks is one method of sub-surface permeability enhancement being investigated by the DOE. Water injected (below the level of the least minimum stress) into a stressed fractured rock system may cause existing fractures to dilate and slip in shear due to a combination of the in situ stress state and the local temperature changes due to water injection, etc.

Dempsey et al (2013) have developed a model of well injectivity evolution caused by shear stimulation within an existing fracture system and applied the model to stimulation of Well 27-15 at Desert Peak geothermal field, Nevada. Their simulations were judged adequate of the injectivity evolution in certain field scale scenarios studied. As Rinaldi et al (2014) point out that the hydroshearing concept is not new, and cite references back to the 1980's. For hydroshearing the injection pressure is below the minimum principal stress. Hydroshearing process depends on many in-situ and operational parameters, for example stress state, fracture properties and intact mechanical, thermal, and hydrologic properties, as well as chemical phenomena. Ghassemi et al., 2007; Safari and Ghassemi (2015); Rinaldi et al (2014) each developed models to simulate of hydroshearing on the field scale, the latter obtained input parameters through analysis of the AltaRock project (Cladouhos et al. 2009, 2011, 2012), and the former represented a more generic study of fractured reservoir response to fluid injection. Flow through fractured rock systems has been studied extensively in the laboratory, for example Lee and Cho (2002).

Cool water introduction to a hot stressed fracture surface is integral to hydroshearing in the geothermal environment (Ghassemi and Tao, 2016) with the introduction of make-up water as hot water is harvested for energy production. We present results of an experimental/numerical study which evaluates this phenomenon observation and analysis of the effect of flow of cool water along a hot, saturated, stressed smooth fracture.

2. EXPERIMENTAL SYSTEM

An experimental test system was developed which can be used to simulate reasonable downhole EGS environmental conditions. It is capable of subjecting jacketed rock specimens with simulated fractures to high temperature, elevated confining pressure, and differential stresses, and high pore-water pressures. Pretest analyses indicated that in order to produce slip by water flow, a temperature difference of about 100°C would be needed between the hot stressed rock and the flowing fluid/water.

The test temperature was chosen as 175°C; this temperature is in the EGS temperature range, and allows for the 100°C temperature difference to be achieved by inflowing room temperature water (with some room for error in the calculated temperature difference).

The confining pressure was chosen as 20.7 MPa, simulating a depth of about 1 km (in the range of EGS). In the tests run, differential stress and pore pressure are parameters varied in the experiments run.

The test system needed to be able to achieve the test conditions stated, and be able to maintain these conditions for extended times (weeks to months). This long test condition time was needed because the test system was time consuming and laborious to set-up, achieve temperature, pressure, and stress conditions, and to conduct the tests. And, as a consequence, we desired to obtain as much data as possible from an individual sample.

We used was an in-house built creep test system (Figure 1) already capable of maintaining the above temperature, stress, and pressure conditions, except the flow through pore pressure capability, which we successfully added. The test system is controlled with a computer-based interfaced system and simultaneously controls the test and acquires test data at user specified time-based intervals. Data collection rates are high (1 sec) for test active testing and low (1 min) for quiescent times.

The testing system consists of a reaction frame that generates the axial force by reacting against a hydraulic cylinder located at the base of the frame, and a pressure vessel that houses specimens during testing. The reaction frame system is capable of applying loads of up to 450 kN. The pressure vessel is rated to 70 MPa and is equipped with electrical band heaters capable of maintaining test temperatures up to approximately 250°C. Silicon oil is used as the confining medium. Fluid confining pressures are coarsely adjusted using an air-assisted pump and finely adjusted and maintained constant using a dilatometer system that either injects or withdraws oil from the vessel. Vessel pressures are measured by a pressure transducer plumbed into the hydraulic line leading from the vessel to the dilatometer. Axial loads applied by the hydraulic cylinder are measured by a load cell located directly above the cylinder in line with the axial push-rod that extends into the pressure vessel and applies axial load to the ends of the specimen. Test temperature is recorded by two thermocouples, one located near the top of the pressure vessel and other near the vessel midheight. Water temperatures are measured using thermocouples strapped to the high pressure tubing leading into and out of the pressure vessel.

Pore fluid pressures (using water as the permeant) are created using two opposing ISCO pumps (maximum pressure 25.9 MPa) plumbed into the top and bottom of the sample.

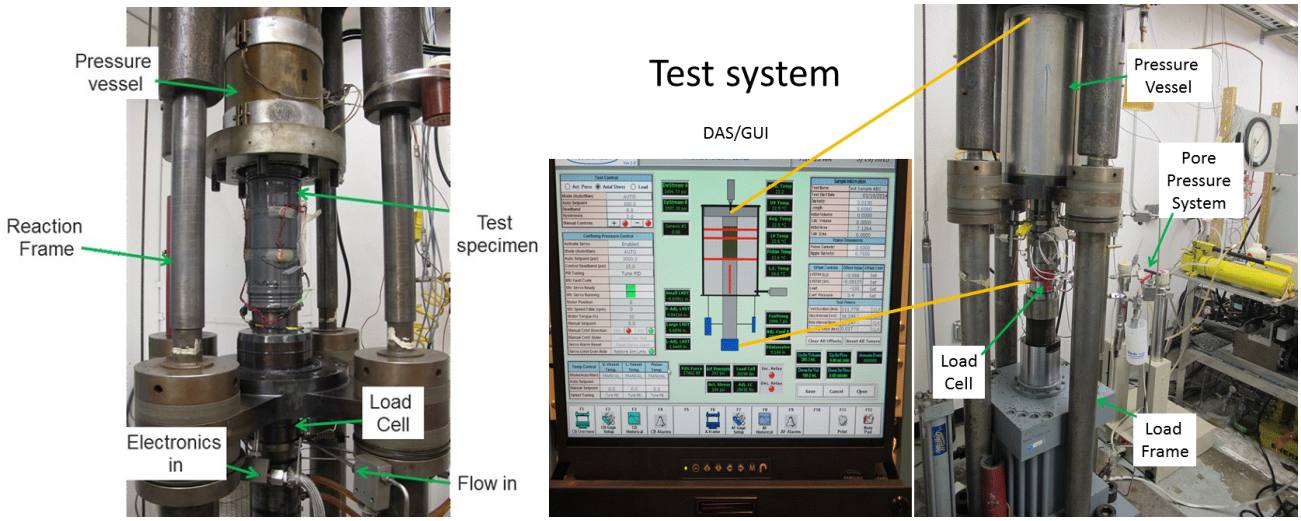

Figure 1: Test set up showing test specimen, pressure vessel, reaction frame and load cell, data acquisition system/graphical user interface and test sample, pressure vessel, load frame and pore pressure system.

Sample displacements are measured using external displacement transducers (LVDTs). Axial displacement was measured by two independent LVDTs within their linear range (0.254 cm and 2.54 cm) that tracked the displacement of the axial push-rod relative to the bottom of the pressure vessel. The external pressure vessel measurements were compared to internal pressure vessel displacements using a pair of internal 2.54 cm LVDTs at 100°C. This displacement was a direct measure of the axial displacement of a specimen because non-specimen deformations were negligible given the imposed constant stress condition. During the tests, the 0.254 cm range LVDTs were reset periodically when the range was exceeded.

2.1 Calibration

Data collected in the experimental study included force, pressure, temperature, displacement, and volume change. Typically, these data are acquired using electronic transducers in which the electrical output is proportional to the change in the measured variable. In all cases, the constants of proportionality were determined through calibration using standards traceable to the National Institute for Standards and Technology.

2.2 Specimen Assembly Details

Specimens are right circular cylinders of Westerly granite with a 30° precut and ground surface. The precut surface is surface ground and then lightly sand blasted to produce some minor roughness, quantified using optical profilimetry methods (Figure 2). The precut rock cylinder is cored with a 0.635 cm diameter hole to opposing sides of the sawcut (Figure 3). The sample assembly is jacketed in thick lead. This allows the sample to "shear" without a jacket leak and for the jacket to function at high temperature (keeping pore fluid in and confining pressure out). The lead jacket has low strength at this temperature.

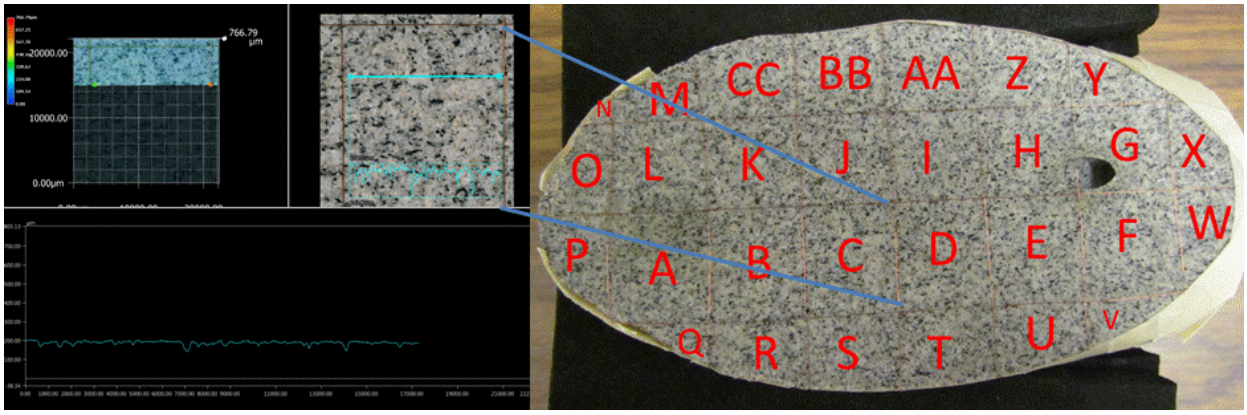

Figure 2: Image of gridded shear surface and surface profile.

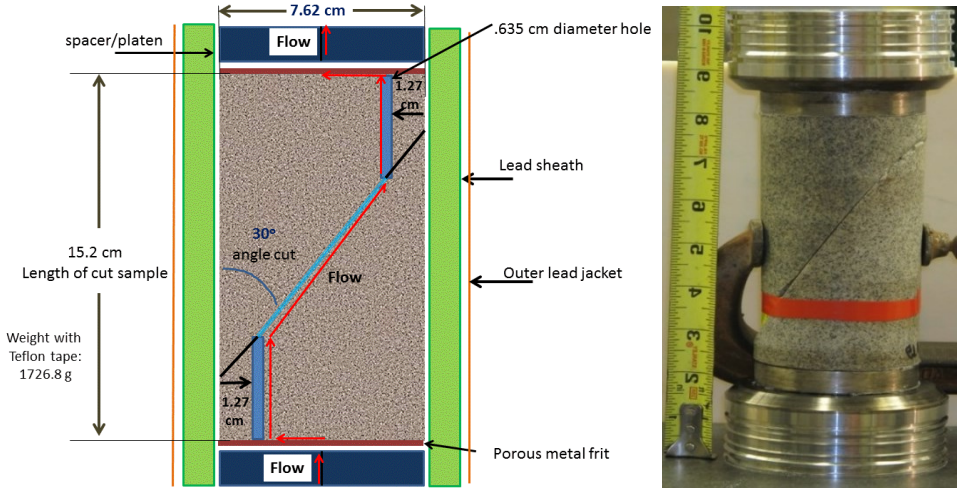

Figure 3: Sample schematic showing approximate dimensions, jacketing system, and flow path.

Figure 4 show the sawcut surfaces of Westerly granite, approximately 7.62 cm diameter and 15.2 cm in length when assembled. The porous frits are pressed metal, allowing fluid access across the entire sample. The end spacers are hardened steel and the end caps are specially designed for metal-metal sealing at elevated temperatures. The fully assembled samples also show positioning of acoustic emission transducers.

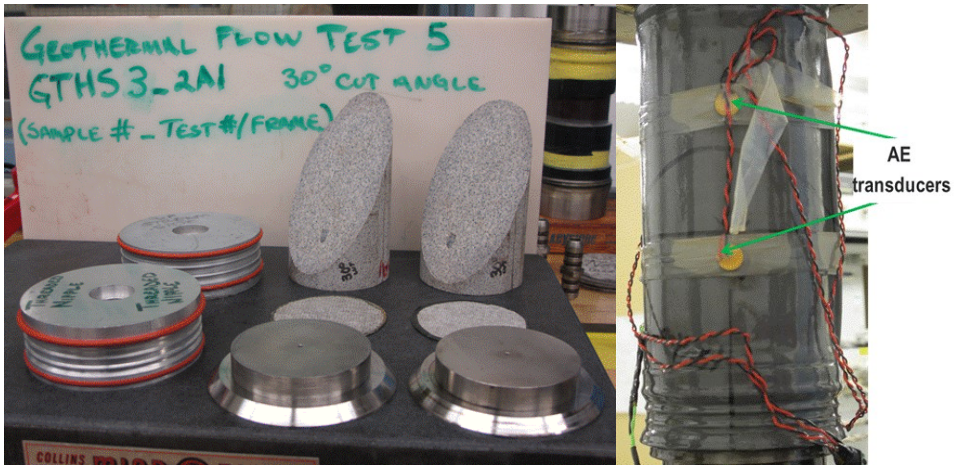

Figure 4: Specimen assembly parts and assembly.

To begin testing the specimen assembly was placed inside the pressure vessel, which was then filled with silicon oil. The pressure in the vessel was increased to the target level (3000 psi) and allowed to stabilize. The sample was then subjected to 1500 psi pore pressure

and forced through the sample as a plumbing check. The vessel was then heated to the target temperature (1°C /min) by activating band heaters located on the outside of the pressure vessel and either clamped to or housed inside the piston. The temperature was allowed to stabilize for approximately 24 hours. After temperature stabilization was completed, sample was allowed to equilibrate for a few days. Samples are generally in the pressure vessel for 30-60 days.

Figure 5 is a plot which shows an example of how a test is conducted (this and all tests were run at 175°C). The primary y-axis plots confining pressure, pore pressure and differential stress versus time. The data shows a constant confining pressure of 3000 psi maintained for this time interval. The differential stress was also maintained at a constant value of 1000 psi. Pore water pressure at the start of the test is 2600 psi, and no flow is observed. At approximately 6000 s, the downstream pressure is dropped, and maintained at 2500 psi. This action caused flow from one side of the sample to the other, scaled on the secondary axis versus time. Flow rate initially increases, then decreases with increasing time. The flow allowed room temperature water (from one of the ISCO pumps) to flow through the sample. The exit temperature is on the order of 100°C (measured by a thermocouple strapped to the downstream pore pressure high pressure tubing).

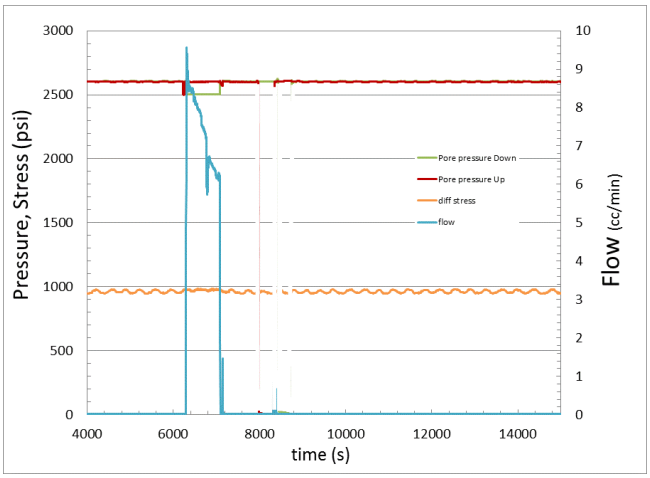

Figure 5: Test conditions and parameters.

Figure 6 is a plot of example test data for approximately 30,000 seconds of test time. The primary y-axis plots pore water pressure and differential stress versus time (confining pressure was held constant at 3000 psi). The differential stress was systematically varied, and the absolute pore pressure was systematically varied; these variations produced different effective stress states to evaluate. For the differential stress of 1000 psi, a flow event was caused by a difference in pore pressures, this resulted in axial displacement at the time of flow. For the differential stress of 1200 psi, a flow event was again caused by a difference in pore pressures, this resulted in axial displacement at the time of flow. Flow rate increases and then decreases with increasing time allowing room temperature water (from one of the ISCO pumps) to flow through the sample. The exit temperature of the water is on the order of 100°C (measured by thermocouple strapped to the exit port).

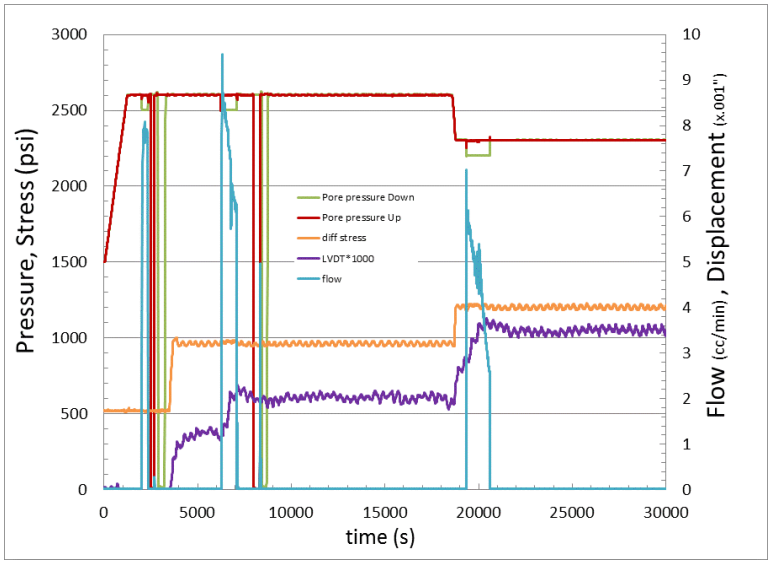

Figure 6: Example test output.

3. NUMERICAL ANALYSIS METHODS

To simulate the core flow test, poro-thermoelastic finite element model is employed to capture the effects flow and thermal diffusion in the intact porous rock on rock matrix and fracture deformation. For the mechanical response of the fracture surface, zero thickness contact interface element model is used to simulate the fracture contact and slip. The fluid flow and thermal conduction in the fracture are modeled by volumetric interface element.

3.1 Poro-thermoelastic Model for Intact Porous Media

Multiple physical processes are involved in the core flow test and contribute to fracture slip. It is crucial for a model to capture all the key physical processes including mechanical behaviors of the rock, fluid flow and thermal diffusion through the fracture and the rock matrix. Based on the constitutive relations, static equilibrium and mass conservation and transportation function, the governing equations representing the fully coupled poro-thermoelastic behavior are derived and written in terms of displacement $\mathbf{u}$, pore pressure p and temperature T :

$$G\nabla^2\mathbf{u} + \frac{G}{1-2\nu}\nabla(\nabla\cdot\mathbf{u}) - \mathbf{m}(\alpha\nabla p + \gamma_1\nabla T) = 0 \tag{1}$$

$$-\alpha(\nabla\cdot\dot{\mathbf{u}}) - \frac{1}{M}\dot{p} + \frac{k}{\mu}\nabla^2 p - \gamma_2\dot{T} = Q_i\delta \tag{2}$$

$$\dot{T} - c^T\nabla^2 T = 0 \tag{3}$$

where G is the shear modulus and ν is the Poisson ratio. α is the Biot's coefficient, k is intrinsic permeability and μ is the fluid viscosity, M is the Biot modulus defined as the fluid contents increase results from the unit increase of pore pressure under constant volumetric strain , Q_i is injection rate at point source, δ is Kronecker delta function, $\mathbf{m} = [1,1,1,0,0,0]^T$ for 3D problems and $\mathbf{m} = [1,1,0]^T$ for 2D problems since the coupling term $\mathbf{m}\alpha\nabla p$ is only active in case of volumetric change of porous solid.

In the following, the finite element formulation for the problem of poro-thermoelastic model is presented. The field equations (1), (2) and (3) are spatially discretized by approximating the field variables of displacement, $\mathbf{u}$, pore pressure p , temperature T , through interpolation functions written as:

$$\mathbf{u} = \mathbf{N}_u\tilde{\mathbf{u}} \qquad p = \mathbf{N}_p\tilde{\mathbf{p}} \qquad T = \mathbf{N}_T\tilde{\mathbf{T}} \tag{4}$$

where $\mathbf{N}_u$ $\mathbf{N}_p$ and $\mathbf{N}_T$ are the shape functions for displacement, pore pressure and temperature respectively. $\tilde{\mathbf{u}}$, $\tilde{\mathbf{p}}$ and $\tilde{\mathbf{T}}$ are the nodal displacement, pore pressure and temperature.

Using Galerkin's method, the weak form of equation system can be derived as

$$\mathbf{K}\dot{\tilde{\mathbf{u}}} - \mathbf{A}\dot{\tilde{\mathbf{p}}} - \mathbf{V}\dot{\tilde{\mathbf{T}}} = \dot{\tilde{\mathbf{f}}} \tag{5}$$

$$-\mathbf{A}\dot{\tilde{\mathbf{u}}} - (\Delta t\theta\mathbf{H}_H + \mathbf{S})\dot{\tilde{\mathbf{p}}} + \mathbf{N}\dot{\tilde{\mathbf{T}}} = \Delta t\theta\mathbf{H}_H\tilde{\mathbf{p}}_{t_{n-1}} + \dot{\tilde{\mathbf{q}}} \tag{6}$$

$$-(\mathbf{R} + \theta\Delta t\mathbf{U})\dot{\tilde{\mathbf{T}}} = \Delta t\mathbf{U}\tilde{\mathbf{T}}_{t_{n-1}} \tag{7}$$

where

$$\mathbf{K} = \int_{V_e}\mathbf{B}^T\mathbf{D}\mathbf{B}\,dV \qquad \mathbf{A} = \int_{V_e}\mathbf{B}^T\alpha\mathbf{m}\mathbf{N}_p\,dV \qquad \mathbf{V} = \int_{V_e}\mathbf{B}^T\gamma_1\mathbf{m}\mathbf{N}_T\,dV \qquad \mathbf{S} = \int_{V_e}\mathbf{N}_p^T\frac{1}{M}\mathbf{N}_p\,dV$$

$$\mathbf{H}_H = \int_{V_e}(\nabla\mathbf{N}_p)^T\frac{k}{\mu}(\nabla\mathbf{N}_p)dV \qquad \mathbf{R} = \int_{V_e}\mathbf{N}_T^T\mathbf{N}_T\,dV \qquad \mathbf{U} = \int_{V_e}(\nabla\mathbf{N}_T)^T c^T(\nabla\mathbf{N}_T)dV \tag{8}$$

Finally, by integrating the constitutive equations, the equilibrium equation, continuity equation and single phase Darcy's law, the coupled poro-thermoelastic field equations in FEM form are obtained and coded in FORTRAN.

A coupled poro-thermal-elastic interface element model is used in this work to simulation the core flow test aiming at reproducing the fracture flow rate and fracture slip observed in the experimental results.

To capture the mechanical response of a fracture, a zero thickness interface element model is used. The zero thickness interface element is then assigned a virtual thickness to generate volumetric element. The volumetric element is easier to analysis the flow and thermal diffusion since that it using the similar formulation as the continuum element. The Mohr-Coulomb criterion is adopted to capture the

slip of fracture interface. The friction angle θ is the only variable governing the interface constitutive model that is descried mathematically as:

$$f = \|\tau\| - \tan\theta p_N \tag{9}$$

where $\|\tau\|$ is the shear stress norm, and p_N is the normal stress on the interface. If p_N is zero, the interface is out of contact so that $\|\tau\|$ is also zero. **Figure** 7 shows the Mohr-Coulomb type criterion. If the stress state lies under the bold line ($f < 0$), the interface state is considered to be in a stick state. If the stress state lies on the bold line ($f = 0$), the interface state is considered to be in a slip state.

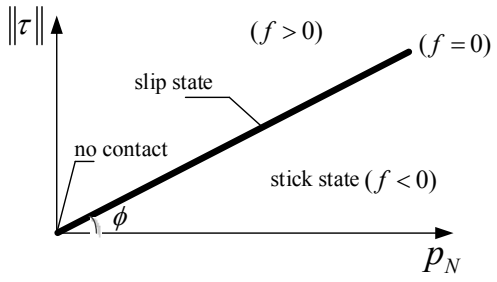

Figure 7: Mohr-Coulomb type criterion.

In this work, 3D 4-node tetrahedron element is employed. Therefore triangle elemental surface on the interface boundary will be duplicated to generate the 6-node zero thickness interface element shown. By adding virtual thickness to zero thickness interface element, a triangular prism volume is generated to simulate the fluid flow and thermal diffusion.

4. NUMERICAL MODELING CORE TEST

4.1 Problem Geometry and physical parameters

This section involves a poro-thermo-elastic analysis of a lab experiment in which a Westerly granite core specimen is subjected to room temperature water injection. The goal is to simulate and compare with the experimental data. **Figure** 8(a) shows the circular cylinder sample geometry with 7.62 cm diameter, and 15.2 cm in length. Two 0.635 cm boreholes are drilled on the top and bottom of sample. An inclined precut fracture is shown in **Figure** (a). 527625 3D tetrahedron elements and 104192 nodes are generated for porous media is shown in **Figure** 8(b). Figure 9 shows the mesh scheme for fracture interface. 29310 interface elements and 2×14888 nodes are on the fracture interface. The poro-thermo-elastic parameters for Westerly granite are shown in the Table 1.

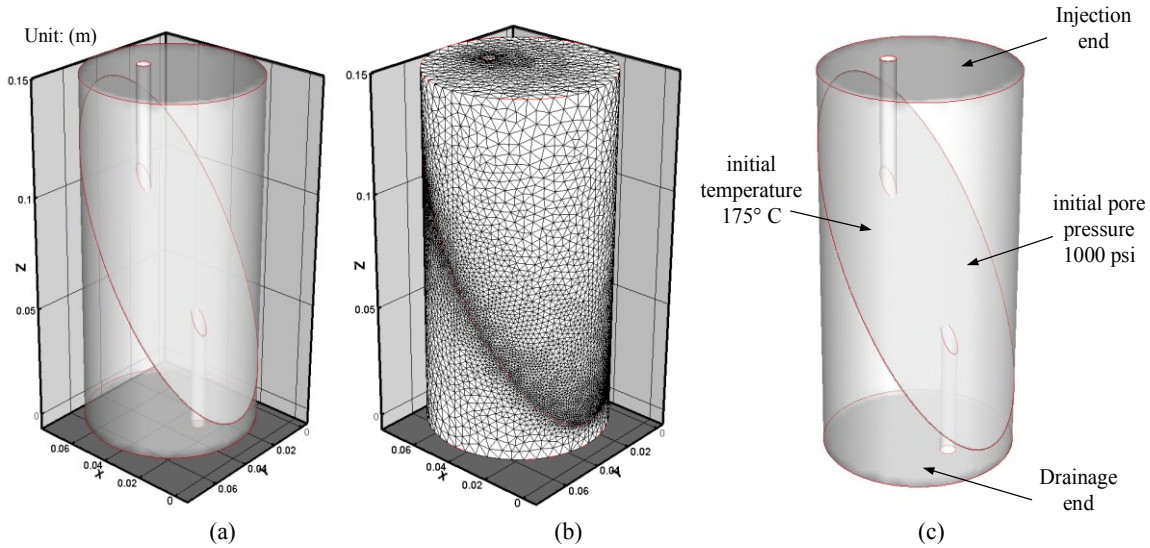

Figure 8: (a) Problem geometry; (b) mesh scheme; (c) experimental sets.

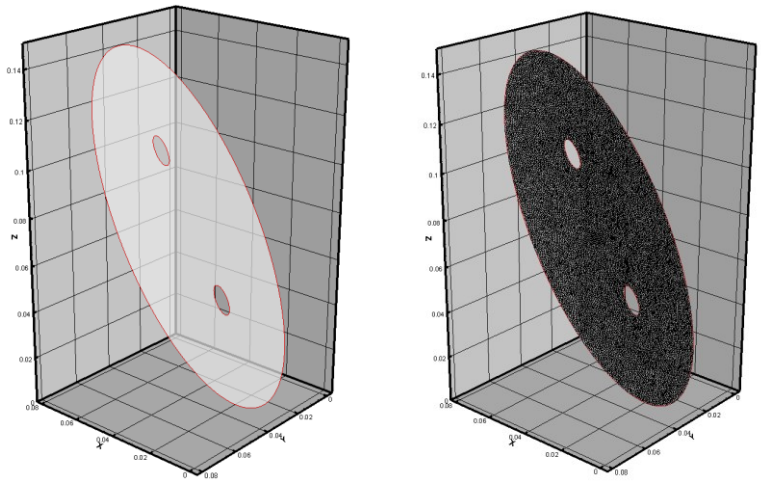

(a) (b)

Figure 9: (a) Fracture interface geometry; (b) mesh scheme.

In this test, the confining pressure was 3000 psi. The initial pore pressure and temperature in the sample were 1000 psi and 175 C. The pore pressure on the sample ends and the boreholes are changed as shown in **Figure 1**(a) according to experimental data shown in Figure . The initial temperature of the sample is °C and it is fixed on the sample surface to simulate a constant temperature boundary. During the simulation, the temperature at the upstream surface and borehole is held at 20 °C.

Poro-thermo-elastic parameters of Westerly granite	
Young's modulus, E	37.5 GPa
Biot's coefficient, α	0.44
Drained Poisson's ratio, ν	0.25
Undrained Poisson's ratio, ν_u	0.33
Permeability coefficient, k	$4 \times 10^{-19} m^2$
Porosity, ϕ	0.2989
Skempton's coefficient, B	0.81
Fluid viscosity, μ	$3 \times 10^{-4} pa \cdot s$
Fluid diffusivity, c	$7 \times 10^{-5} m^2 / s$
Thermal expansion coefficient of solid, α_m	$1.8 \times 10^{-5} K^{-1}$
Thermal expansion coefficient of fluid, α_f	$3.0 \times 10^{-4} K^{-1}$
Thermal diffusivity, c^T	$7.4 \times 10^{-7} K^{-1}$
Parameters of fracture interface	
Fracture thickness, h	0.003937 inch
Fracture permeability, k_f	$6.1559 \times 10^{-13} m^2$
Fracture normal stiffness, K_N	$10 \times 10^{13} N / m$
Fracture shear stiffness, K_T	$10 \times 10^{10} N / m$
Frictional angle, θ	30°

Table 1. Poro-thermo-elastic parameters for Westerly granite and fracture surface.

4.2 Numerical Results

Figure 1 and **Figure 1** show the comparison between the numerical results and experiment data. By comparison, the numerical results are in reasonable agree with the experiment data. The flow rate increases when fluid pressure of the lower end is lowered by 100 psi. The sample displacement includes both an elastic deformation of the solid and slippage on the fracture. **Figure 1** shows the comparison between numerical analysis and experiment data for the top surface displacement. It can be seen that one of major causes of the top displacement is the increment of the differential stress from 520 psi to 980 psi and then to 1200 psi. Another factor that causes slip is the cool fluid flow. Slip increases with the flow rate jump. The mechanism includes the pore pressure change, cooling by convection and more importantly, the normal and shear stress change on the fracture surfaces and will be detailed illustrated in the following discussion.

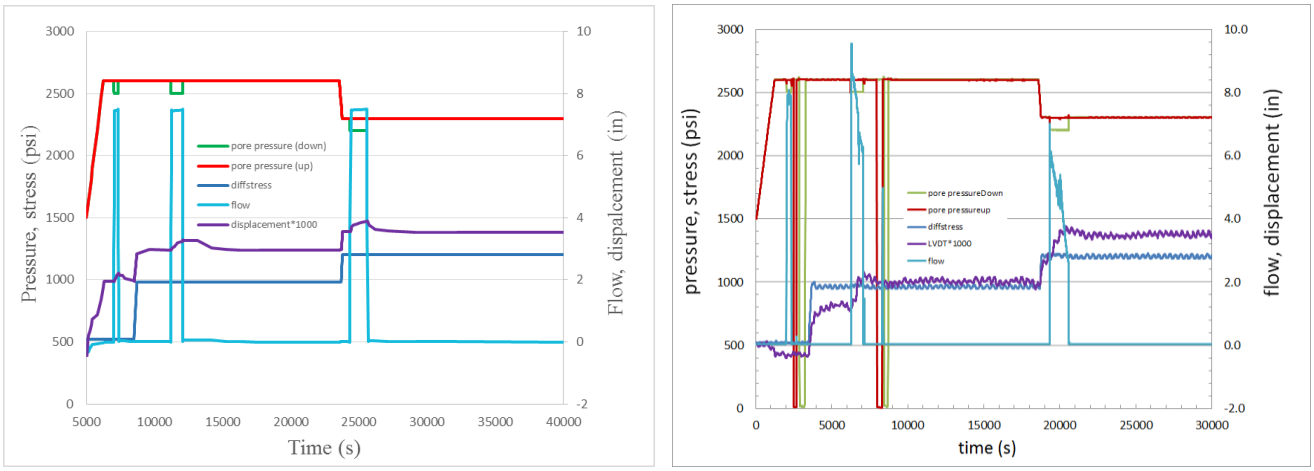

(a) (b)

Figure 10: Flow and top displacements results comparison: (a) numerical simulation results and (b) experiment data (the right axis value is to be multiplied by 0.001).

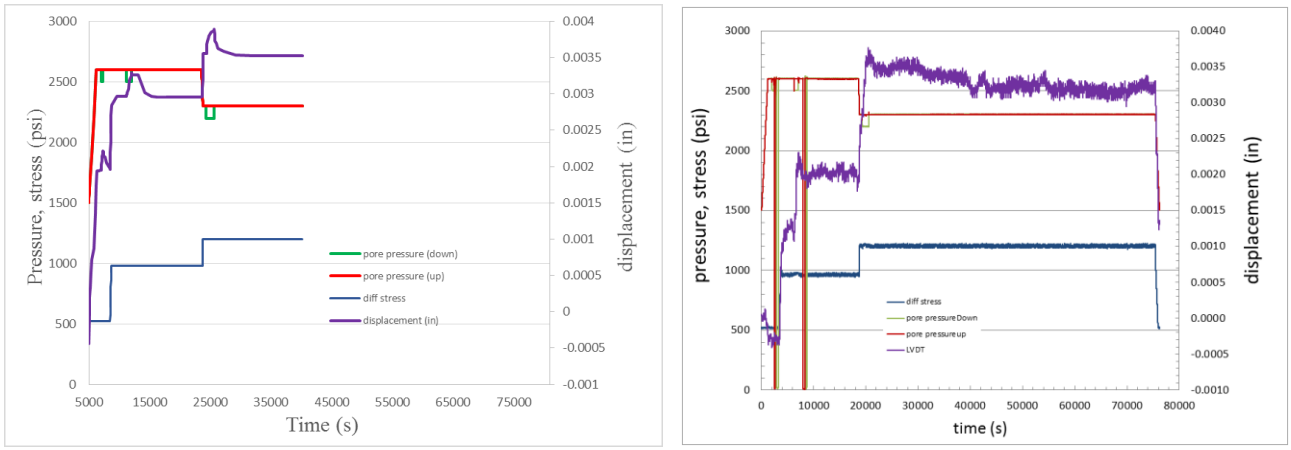

(a) (b)

Figure 11: Top displacements results comparison: (a) numerical simulation results and (b) experiment data.

Figure shows the initial mesh and final deformation amplified by 100 times, which shows the major contributor to the top end displacement is the slip on the fracture surface.

Figure has time indicators to help guiding visualization of the results. **Figure** shows the temperature contours for the middle slice through the sample and for the fracture surface. **Figure** (a) shows the temperature distribution at time ① right before the flow rate increase. **Figure** (b) shows the temperature change after the cold fluid flows through the fracture surface to the lower borehole at time ②. The temperature of fracture surface and adjacent rock has decreased by the convection effect of cold fluid flow. The downstream temperature from the figure is 130℃ at the end of flow interval. Fig**ure** 15 is the pore pressure of porous media and fracture surface. Fig**ure** 15(a) shows the uniform pressure of 2600 psi at time ①. Fig**ure** 15(b) shows the pore pressure at time ② when the lower end pressure decrease from 2600 psi to 2500 psi. The pressure difference between the upper and lower ends induces the flow, rock cooling, and stress changes on the fracture surface.

Figure 16 displays the fluid pressure, temperature, normal stress, shear stress on the fracture surface and the fracture state (stick-slip) during the downhole pressure drop intervals for different stages. The purpose here is to better illustrate the coupled effects in the whole system. In the 1st flow interval (time ①-②), the 1st column is the fluid pressure on the fracture surface before and after 100 psi pressure decrease on the lower end. The 2nd column shows the temperature contour. After cold fluid flows through the fracture, the region between the two boreholes is cooled. The outlet temperature (at lower borehole) is approximately 130˚C. In the 3rd column, the normal stress around the upper borehole is lowered due to the shrinkage of the cooled rock round the upper end. Hence, a lower normal stress is also found in the cooled region between the two boreholes. Because of the lower normal stress caused by cooling, the fracture state in the area between the two boreholes changes to slip (red color in the stick-slip state contour in the 5th column). This is the major cause of slip during the flow intervals. The shear stress contours are displayed in the 4th column. Similar comparisons are made for the 2nd and 3rd downstream pressure drop intervals. The physical phenomenon are similar. The shear stress gradually increases since the differential stress increases from 520 psi in the1st interval to 980 psi in the 2nd interval and finally to 1200 psi in the 3rd interval.

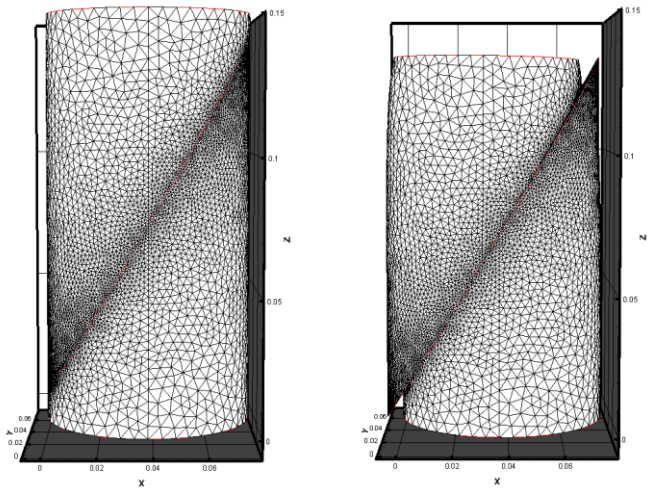

Figure 12: (a) Initial geometry; (b) deformed mesh amplified by 100 times at the end of experiment.

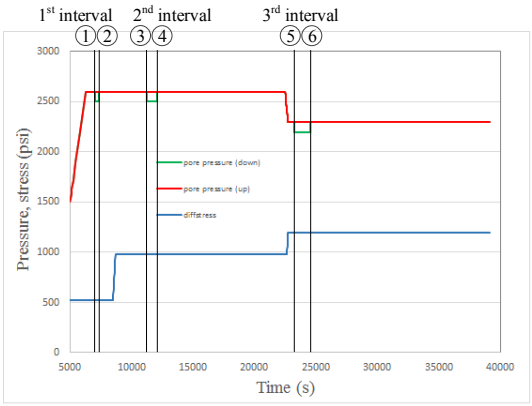

Figure 13: Time indicators for results visualization.

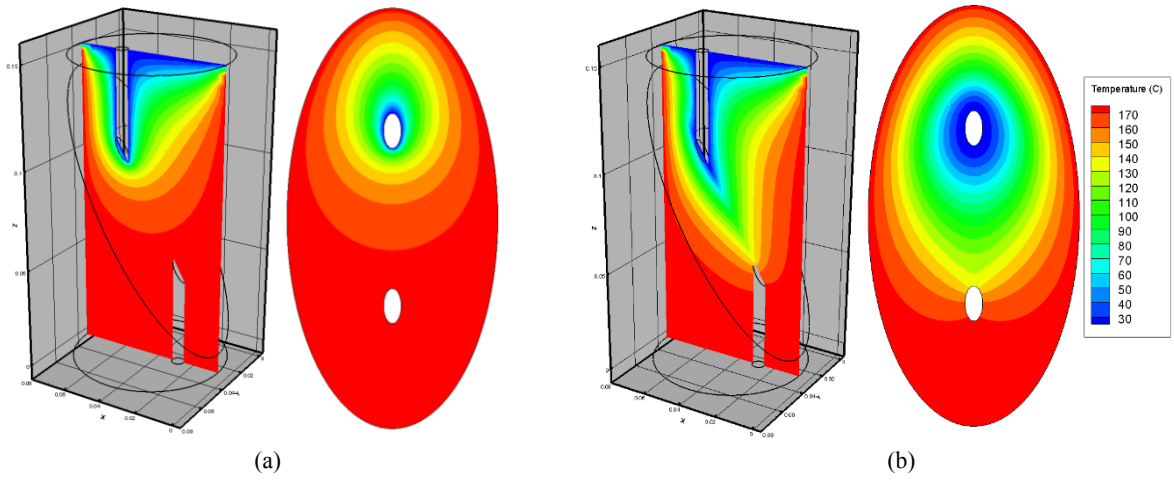

Figure 14: Temperature contour on middle slice and fracture surface at (a) time ① and (b) time ②.

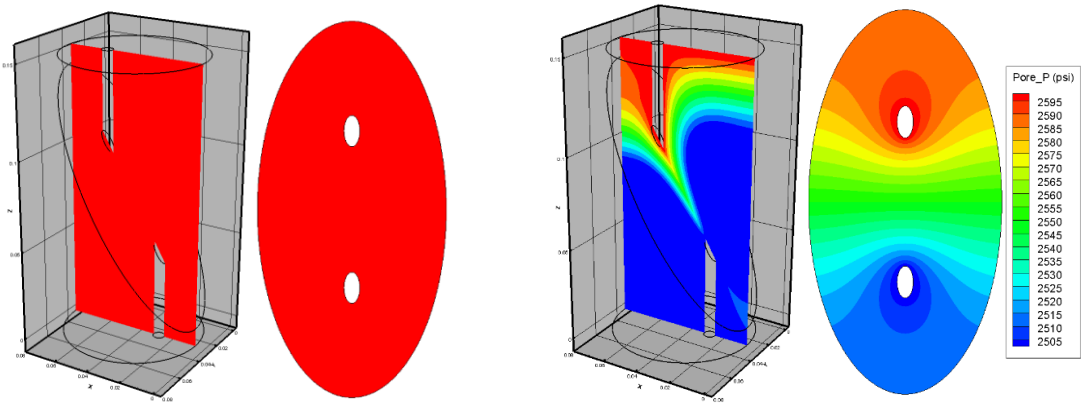

(a) (b)

Figure 15: Pore pressure contour on middle slice and fracture surface at (a) time ① and (b) time ②.

	(a). 1st downhole pressure drop (time ①-②)				
time	Fluid pressure (psi)	Temperature (C)	Normal stress (Pa)	Shear stress (Pa)	Stick-slip states
①	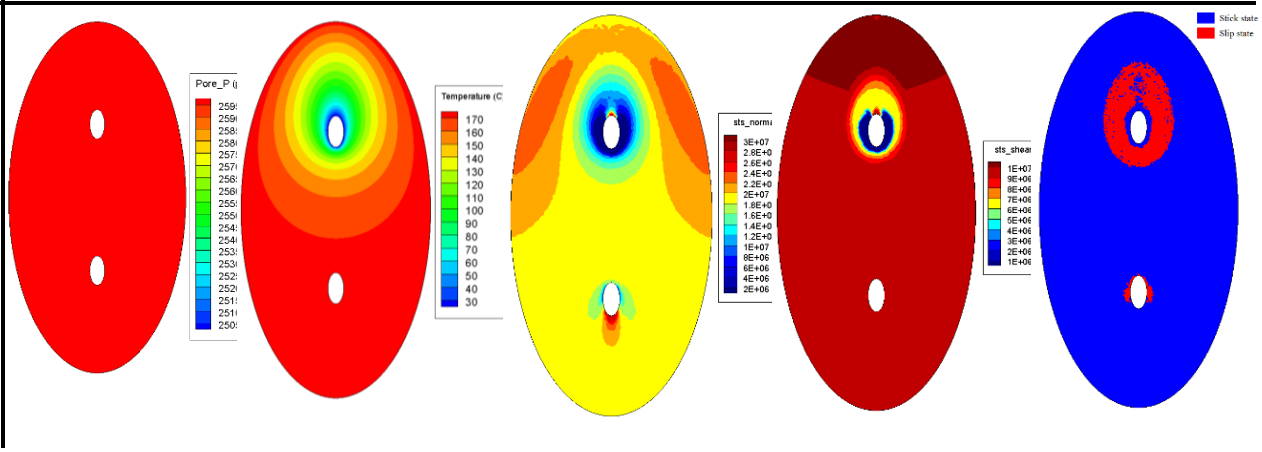				

②	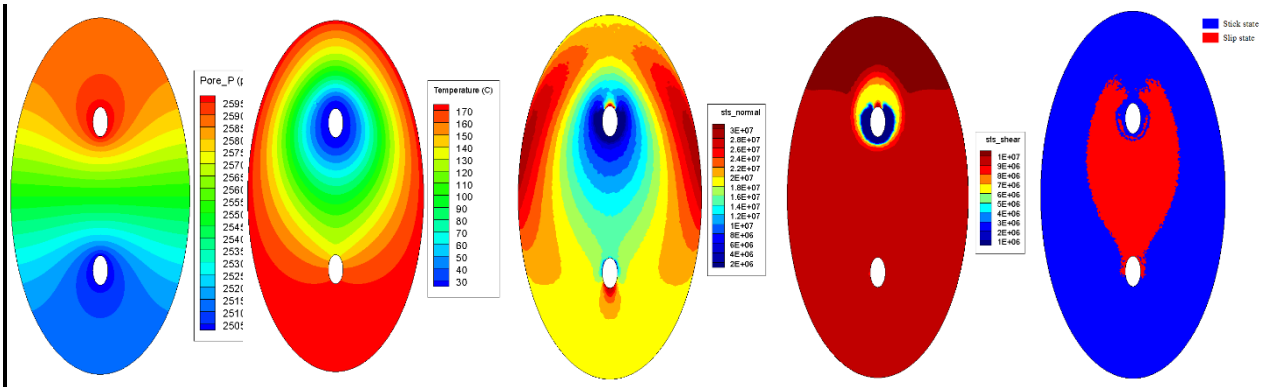				
	(b). 2nd downhole pressure drop (time ③-④)				
time	Fluid pressure (psi)	Temperature (C)	Normal stress (Pa)	Shear stress (Pa)	Stick-slip states
③	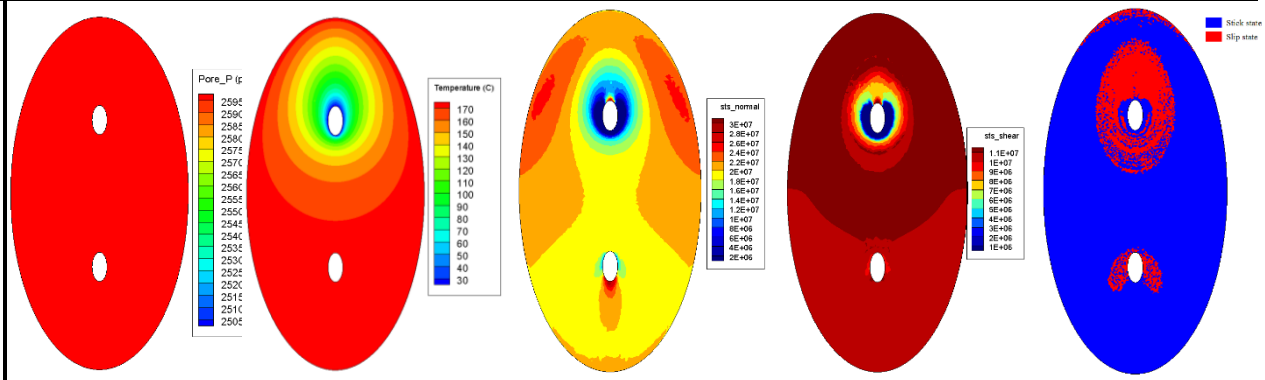				
④	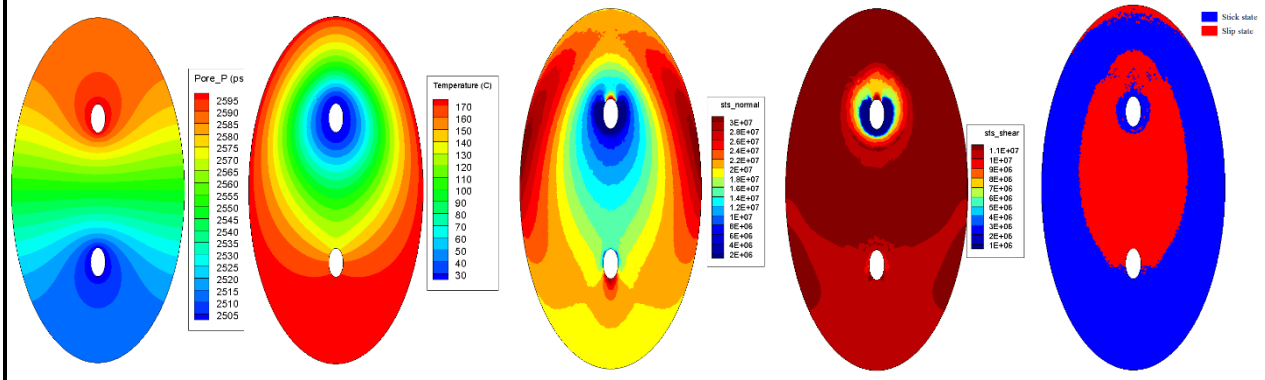				
	(c). 3rd downhole pressure drop (time ⑤-⑥)				
time	Fluid pressure (psi)	Temperature (C)	Normal stress (Pa)	Shear stress (Pa)	Stick-slip states

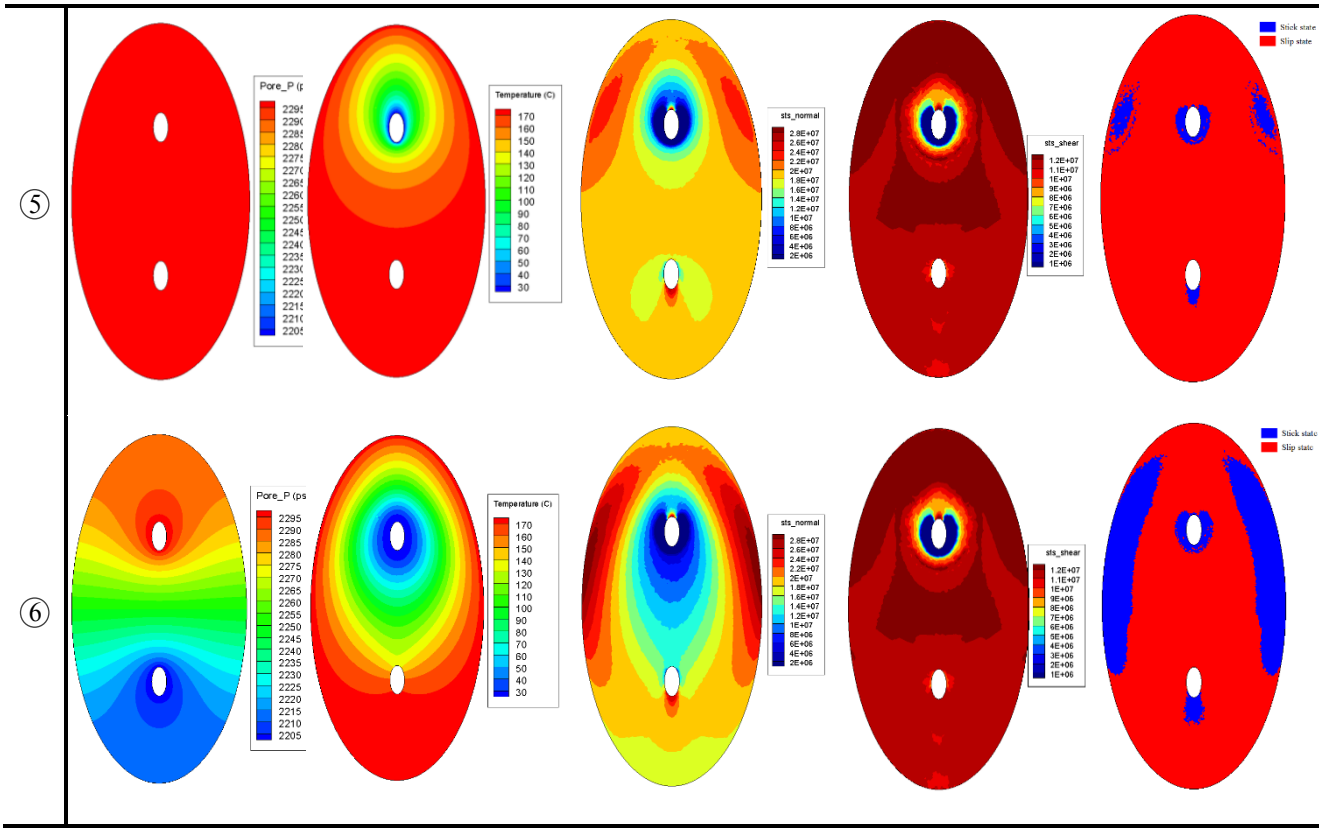

Figure 16: Contours of fluid pressure, temperature, normal stress, shear stress, stick-slip states on the fracture surface during (a) 1st downstream pressure drop interval (time ①-②); (b) 2nd downstream pressure drop interval (time ③-④); (c) 3rd downstream pressure drop interval (time ⑤-⑥).

DISCUSSION AND CONCLUSIONS

This work presents the results of a coupled experimental and numerical effort to develop a technique to conduct, observe and measure shear displacement resulting from introduction of cool water to a hot wet stressed fracture.

For specific differential stress the experiments are being successfully modeled. The analysis effort has developed a method to model, observe and determine heat transfer, fluid flow and shear displacement shear displacement resulting from introduction of cool water to a hot wet stressed fracture.

We note that flow was initiated in some test by water flow induced by a pore pressure decrease on the downstream side of the sample. This action decreases the average pore pressure imposed on the sample, and from afar increases the normal stress on the fracture surface. Slip is sometimes observed. Possible mechanisms which could account for the slip include heating/thermal expansion of inflowing water which would force opposing rock surfaces apart; and cooling of opposing rock surfaces, resulting in a decrease in the real area of contact. These mechanisms are being studied through the numerical analyses.

ACKNOWLEDGEMENTS

This work was supported by the US Dept. of Energy Geothermal Technologies Office; the authors would like to thank Lauren Boyd and Sean Porse for their interactions, reviews and support of this work. Sandia National Laboratories is a multi-program laboratory managed and operated by Sandia Corporation, a wholly owned subsidiary of Lockheed Martin Corporation, for the U.S. Department of Energy's National Nuclear Security Administration under contract DE-AC04-94AL85000. SAND2016-1274 C

REFERENCES

Cladouhos, T.T., Clyne, M., Nichols, M., Petty, S., Osborn, W.L., Nofziger, L.: Newberry Volcano EGS Demonstration Stimulation Modeling. *GRC Trans*. 35, 317–322 (2011).

Cladouhos, T.T., Osborn, W. L., Petty, S., Bour, D., Iovenitti, J., Callahan, O., Nordin, Y., Perry, D., Stern, P.L.: Newberry Volcano EGS Demonstration—Phase I Results. Proceedings of 37th Workshop on Geothermal Reservoir Engineering, Stanford, CA, (2012).

Cladouhos, T.T., Petty, S., Larson, B., Iovenitti, J., Livesay, B., Baria, R.: Toward More Efficient Heat Mining: A Planned Enhanced Geothermal System Demonstration Project. *GRC Trans*. 33, 165–170 (2009).

Dempsey, D., Kelkar, S., Lewis, L., Hickman, S., Davatzes, N., Moos, D., Zemach, E.: Modeling Shear Stimulation of the Desert Peak EGS Well 27-15 Using a Coupled Thermal-Hydrological-Mechanical Simulator, ARMA (2013).

Ghassemi, A., Tarasovs, S., and Cheng, A. H.-D. 2007. A Three-dimensional Study of the Effects of Thermo-mechanical loads on Fracture Slip in Enhanced Geothermal Reservoir. Int. J. Rock Mechanics & Min Sci., Vol. 44 , pp. 1132–1148

Lee, H.S., Cho, T.F.: Hydraulic Characteristic of Rough Fractures in Linear Flow under Normal and Shear Load. *Rock Mech. Rock Eng.* 35(4), 299–318 (2002).

Rinaldi, A.P., Rutqvist, J., Sonnenthal, E.L., Cladouhos, T.T.: Coupled THM Modeling of Hydroshearing Stimulation in Tight Fractured Volcanic Rock, *Transport in Porous Media*, DOI: 10.1007/s11242-014-0296-5, (2014).

Cerfontaine, B., Dieudonné, A. C., Radu, J. P., Collin, F., & Charlier, R.. 3D Zero-thickness Coupled Interface Finite Element: Formulation and Application. Computers and Geotechnics, 69, 124-140 (2015).

Shahrour, I., & Rezaie, F.. An Elastoplastic Constitutive Relation for the Soil-structure Interface under Cyclic Loading. Computers and Geotechnics, 21(1), 21-39 (1997).

Nguyen, V. P.. An Open Source Program to Generate Zero-thickness Cohesive Interface Elements. Advances in Engineering Software, 74, 27-39 (2014).

Ghassemi, A., Tao, Q. 2016. Thermo-Poroelastic Effects on Reservoir Seismicity and Permeability Change. Geothermics Special Issues on EGS (in press).